This document is downloaded from the
VTT's Research Information Portal
https://cris.vtt.fi

VTT Technical Research Centre of Finland

Estimation of boreal forest floor reflectance from airborne hyperspectral data of coniferous forests

Markiet, Vincent; Mõttus, Matti

Published in:
Remote Sensing of Environment

DOI:
10.1016/j.rse.2020.112018

Published: 01/11/2020

Document Version
Publisher's final version

License
CC BY-NC-ND

Link to publication

Please cite the original version:
Markiet, V., & Mõttus, M. (2020). Estimation of boreal forest floor reflectance from airborne hyperspectral data of coniferous forests. *Remote Sensing of Environment*, *249*, [112018]. https://doi.org/10.1016/j.rse.2020.112018

VTT
http://www.vtt.fi
P.O. box 1000FI-02044 VTT
Finland

By using VTT's Research Information Portal you are bound by the following Terms & Conditions.

I have read and I understand the following statement:

This document is protected by copyright and other intellectual property rights, and duplication or sale of all or part of any of this document is not permitted, except duplication for research use or educational purposes in electronic or print form. You must obtain permission for any other use. Electronic or print copies may not be offered for sale.

Download date: 04. May. 2023

Remote Sensing of Environment 249 (2020) 112018

Contents lists available at ScienceDirect

Remote Sensing of Environment

journal homepage: www.elsevier.com/locate/rse

Estimation of boreal forest floor reflectance from airborne hyperspectral data of coniferous forests

Vincent Markiet*, Matti Mõttus

VTT Technical Research Centre of Finland, P.O. Box 1000, Espoo FI-02044 VTT, Finland

ARTICLE INFO

Keywords:
Airborne imaging spectroscopy
Boreal forest
Understory
Forest floor BRF
Site fertility class
Linear spectral unmixing
Sunlit fraction
Hyperspectral imaging
Photochemical reflectance index

ABSTRACT

In open forest canopies, such as in boreal forests, forest floor can contribute significantly to the observed top of canopy reflectance. In order to retrieve the biophysical properties of the tree layer, correcting for forest floor is essential. Traditionally, the algorithms for retrieval of forest floor reflectance depend on tree layer information such as leaf area index, canopy cover, and site fertility. To overcome these circular dependencies, we propose an algorithm that can be applied only using airborne remote sensing data. We acquired airborne hyperspectral imagery over the Hyytiälä forest research station (61°50′N, 24°17′E) in central Finland on July 3rd in 2015 using a hyperspectral pushbroom line scanner. The image data had a spectral resolution of 4.6 nm, and the spatial resolution was 0.6 m. We developed a linear spectral unmixing algorithm, which is based on the definition of the reflectance factor, taking into account the variation of incident irradiance inside the canopy. The weights of the mixture can be computed from tree canopy gap fractions, a tree species insensitive leaf albedo, and average tree stand reflectance. Canopy gap fractions were retrieved with empirical methods available in scientific literature. The forest floor reflectance in the near-infrared increased with site fertility in agreement with the forest floor field measurements. Moreover, we found that in near infrared, the reflectance of moderately rich and moist upland forests was significantly different from all other fertility classes. Finally, we tested the reflectance decomposition on the photochemical reflectance index (PRI) known to be heavily affected by understory reflectance and canopy structure, and the forest PRI to be decoupled from the PRI of the over- and understory.

1. Introduction

Forest floor spectral properties are an important driver of top-of-canopy (TOC) bidirectional reflectance factor (BRF): in forests with open canopies, such as in boreal forests, understory can contribute up to 40% at forest stand level and 20% at landscape level in the red and near-infrared (NIR) parts of the spectrum (Rautiainen et al., 2011). This can cause spectral uncertainty in determining the properties of the forest canopy, such as its leaf area index (LAI) used in carbon balance models, from satellite data (Eriksson et al., 2006; Heiskanen et al., 2012). The forest floor BRF contains information on the forest ecosystem, the growing conditions of the understory vegetation, and soil fertility (Hallik et al., 2009). Moreover, the forest floor BRF can be used to differentiate among understory vegetation species and monitor their physiology (Rees et al., 2004) or determine the fractional cover of major understory plant types similarly found in boreal forest (Schaepman-Strub et al., 2009).

In Finnish boreal forests, forest floor is usually covered by an understory, commonly composed of a ground layer (soil and mosses) and an upper understory layer, which are dwarf shrubs; bare soil is rarely visible (Rautiainen et al., 2011). The understory vegetation varies with the site fertility, light availability, fire regime, etc. and can include ferns, herbs and lichen intermingled with debris and litter. In this paper, we hence use understory and forest floor almost interchangeably, although the latter term is more general and includes the rare situations of a lack of understory. Forest floor also plays a key role in the forest site fertility classification system used in the study: the Finnish national forest inventory is based on forest floor vegetation (Kuusela and Salminen, 1969), making it a natural classifier for studying forest floor reflectance.

One way to measure forest floor BRF is through extensive fieldwork. However, it is time consuming and labor intensive. Mapping forest floor reflectance from air or space is possible, but poses many challenges as understory layers are not homogenous, but rather a spatially varying mixture of the different components. Only a few studies have attempted to create a spectral database of boreal forest understory vegetation, such as Miller et al. (1997) in Canadian boreal forest, Peltoniemi et al. (2005) and Rautiainen et al. (2011) in Finnish boreal forest, and Kuusk

* Corresponding author.
E-mail addresses: vincent.markiet@vtt.fi (V. Markiet), matti.mottus@vtt.fi (M. Mõttus).

https://doi.org/10.1016/j.rse.2020.112018
Received 18 March 2019; Received in revised form 24 July 2020; Accepted 25 July 2020
0034-4257/ © 2020 Published by Elsevier Inc.

et al. (2004) and Hallik et al. (2009) who measured in Sweden and Estonia. Spectral libraries can never achieve the spatial coverage provided by remote sensing techniques. A possible path to separating the over- and forest floor BRF contributions in remote sensed signal is by using (linear) spectral unmixing, where the signal is decomposed into several spectral contributors (endmembers) of known targets (Adams et al., 1986; Peddle et al., 1999; Somers et al., 2011). Linear spectral unmixing has been used frequently in remote sensing of vegetation (e.g. Asner et al., 2004; Fitzgerald et al., 2004; Goodwin et al., 2005; Jiménez-Muñoz et al., 2009; Leboeuf et al., 2007; Peddle et al., 1999; Rogan and Miller, 2006).

Only few studies have attempted to measure forest floor BRF from air or space. Pisek et al. (2010) successfully measured forest floor BRF in a boreal forest from an aircraft using a hyperspectral camera with nadir and one off-nadir view angle (40°). Using linear spectral unmixing they were able to map the background reflectance in forest stands with LAI < 5 with an error within 16% in the red and 12% in NIR. Pisek et al. (2015a) were able to calculate forest floor BRF using an UAV and found the optimal view zenith angles to be 0° and 40° and a solar zenith angle of 45° for mid-summer conditions. More studies have attempted to retrieve forest floor BRF from satellite data. Jiao et al. (2014) used a Multi-angle Imaging SpectroRadiometer (MISR) to calculate forest floor BRF and found the largest variation of forest background reflectivity at middle and high latitudes of the northern hemisphere. Pisek et al. (2015b) used semi-empirical and physical based approaches with MODIS Bidirectional Reflectance Distribution Factor (BRDF) data to track seasonal changes in forest floor Normalized Difference Vegetation Index (NDVI). A similar study by Rautiainen and Heiskanen (2013) tracked the seasonal dynamics of forest floor BRF using a multi-sensor (SPOT, MODIS, Hyperion) time-series approach and showed that the contribution of forest floor to TOC or landscape reflectance strongly depends on tree canopy gap fraction and forest floor reflectance with seasonal variation from 20% to 40%. Suzuki et al. (2011) used a combination of airborne imagery and radiative transfer modelling to estimate the NDVI of forest floor and canopy. Their results indicate that satellite-derived NDVI in boreal forests can be attributed up 85% by the forest floor component. Pisek and Chen (2009) used MISR data to estimate forest floor reflectance from nadir and at 45° forward direction angle. Their study concluded that the background reflectivity varies between coniferous and deciduous stands, particularly in NIR, and cannot be ignored when retrieving canopy biophysical properties. Kuusinen et al. (2015) used a combination of spectral forest floor measurements, tree stand measurements (LAI, canopy cover fraction, site fertility, etc.) and Landsat Thematic Mapper (TM) to calculate the variation in canopy and forest floor reflectance during stand development in Finnish boreal forests. In addition, they used linear spectral unmixing to estimate the BRF of sunlit forest floor, and canopy and shaded ground for sites of different fertility. Their results show that the sunlit forest floor BRF in the NIR increases as site fertility increases but decreases in the RED and shortwave-infrared bands.

One shortcoming of the studies by Jiao et al. (2014), Kuusinen et al. (2015), Liu et al. (2017), Pisek et al. (2015b), Pisek and Chen (2009), Rautiainen and Heiskanen (2013), and Suzuki et al. (2011) is the dependency on field measured information such as site fertility class or canopy gap fraction. Alternatively, forest floor reflectance can be calculated using multi-angular data and forest parameters (Pisek et al., 2010, 2012). However, using this approach still requires tree height, crown height, canopy cover, and needle clumping index as model inputs. The forest floor reflectance retrieval algorithm by Kuusinen et al. (2015) cannot be used to map plot level forest floor BRF and requires numerous field-measured input parameters.

The photochemical reflectance index (PRI) is correlated with the photosynthetic light use efficiency (LUE), the efficiency at which the plants convert light into fixed carbon (Gamon et al., 1992). It is a robust and well-validated indicator at the level of a leaf. In the study on the key spectral features of boreal forest floor by Rautiainen et al. (2011), PRI was the index strongest correlated with the cover fraction of herbs, and it was suggested as a suitable tool for separating fertile and infertile site types. For structured canopies, PRI measured from a distant platform (UAV, aircraft) is heavily affected by forest floor and canopy structure (Barton and North, 2001; Damm et al., 2015; Mõttus et al., 2015). We hence tested the unmixing algorithm on this vegetation index to see if it can bring out the contrasting spectral properties of the different vegetation components.

Therefore, the goals of this study are: 1) to develop an algorithm that allows to determine the forest floor reflectance factor only using airborne remote sensing, and 2) to calculate the forest floor reflectance factor for sites with different fertility classes. To achieve this, we developed a form of the linear unmixing equation that takes into account the variations of irradiance inside the canopy and studied the effect of forest fertility class on remotely sensed forest floor reflectance at different wavelengths.

2. Materials and methods

2.1. Study site

The airborne hyperspectral acquisition covered the area surrounding the Hyytiälä forest research station in central Finland (61°50′N, 24°17′E) managed by the University of Helsinki. The Hyytiälä area is predominantly covered with boreal forest. The forest overstory is composed of three main tree species: deciduous silver birch (*Betula pendula*), evergreen Scots pine (*Pinus sylvestris* L) and evergreen Norway spruce (*Picea abies* (L) Karst). The terrain is hilly with an average elevation of 160 m above sea level and is covered mainly with managed boreal forest, agricultural fields, wet- and peatlands. The forest floor is a mix of bryophyte, lichen species and a collection of shrubs. The climate is of a mild sea climate influenced by the Gulf stream with the growing season lasting from May until late August. Monthly average air temperatures varies from 5 °C in May to 15 °C in late August.

2.2. Airborne hyperspectral acquisition

On July 3rd, 2015 we acquired airborne hyperspectral imagery using an AISA Eagle II airborne hyperspectral scanner (AHS) (Specim-Spectral Imaging Ltd., Oulu, Finland) onboard a Skyvan research aircraft. We operated the flights between 10:44 and 12:20 (GMT + 3) and were flown at approximately 1 km altitude above the ground with flight lines consecutively in the northwestern and southeastern directions to minimize BRF effects. The average solar zenith angle was 48°, the photosynthetic photon flux density ranged from 1285 to 1493 $\mu mol\, m^{-2}\, s^{-1}$ with a mean value of 1408 $\mu mol\, m^{-2}\, s^{-1}$ (SMEAR II measurement data above the forest). The weather conditions were optimal for an airborne hyperspectral acquisition with a clear blue sky. We flew 11 flight lines covering an area of approximately 12 km long and 4.5 km wide.

The Aisa Eagle II sensor is a pushbroom scanner sensitive in the 400–970 nm spectral region. The instrument was configured to have a spectral bandwidth (half width full maximum) of 4.6 nm and 128 contiguous spectral bands. The AHS's field of view (FOV) was 37.7° divided over 1024 pixels with a pixel size of approximately 0.6 m in both along- and cross-track directions. We used an Oxford RT3100 IMU for post-correction of progressive and angular movements. The IMU and AHS were synchronized at the start of each flight line using a synchronization signal in the instrument software.

Each image was radiometrically calibrated using the Caligeo tool (version 4.9.7, Specim OY, Oulu, Finland) based laboratory-measured calibration coefficients. We then used ATCOR-4.7 (ReSe applications Schläpfer, Switzerland) to apply atmospheric correction and convert at-sensor radiances to top-of-canopy (TOC) hemispherical-directional reflectance factors (HDRF). An aerosol optical thickness of 0.06 was measured at 500 nm by a sun photometer at the Hyytiälä forest research

station and was downloaded from the AERONET (aerosol robotic network) website (NASA, 2019). The optical thickness of 0.06 corresponds to a visibility of 120 km in Atcor (Daniel Schläpfer, ReSe Applications, pers. comm.).

We then performed image georegistration and orthorectification using the Parge image rectification tool (version 3.1, ReSe Applications Schläpfer, Switzerland). We downloaded a digital elevation model with 2 m spatial resolution from the Finnish National Land Survey and selected 15 road intersections as ground control points on the atmospherically corrected AISA images. The ground control points were validated for spatial accuracy with an aerial photograph (spatial resolution 0.5 m, Finnish National Land Survey) using the WGS1984 UTM zone 35. This process determined the boresight angles, i.e. the alignment between the IMU axes and the optical axis of the hyperspectral sensor.

Finally, we downloaded a 3D lidar point cloud (0.5 points per m^2) dataset from the National Land Survey of Finland to create a top-of-canopy (TOC) surface for orthorectifying the atmospherically corrected reflectance images. We used the Lastools software (version: 140615, RapidLasso GmbH, Germany) to separate ground and tree canopy returns. We first filtered out all outliers 30 m and higher above the ground. Then we created a digital surface model (DSM) by converting the point cloud to a 10 m grid. We removed any spikes in the DSM by applying two smoothing processes in which we used focal statistics in Arcmap 10 (Esri, Redlands, CA, USA) with a 3 × 3 grid to calculate the mean cell value within this grid. The smoothed DSM was then used as TOC surface when georectifying AHS data using the fast nearest neighbor resampling method onto a 0.6 m pixel grid in the WGS1984 UTM zone 35 coordinate system. The final geometric accuracy of the AHS data was approximately 2 m.

2.3. Forest plot data

We combined plot measurements by Korhonen et al. (2011) and (Majasalmi et al., 2012, 2015) including information on plot location (easting, northing), site fertility class, tree species composition, diameter at breast height (DBH), median tree height, and effective leaf area index (LAI) calculated from canopy gap fraction (CGF). The study sites belonged to the following fertility classes in decreasing order of fertility: moderately-rich upland, moist upland, dryish upland, and dry upland (Rantala et al., 2011). We visually checked each field plot if it had been harvested in the AHS imagery and excluded 92 field plots which had changed between 2008 and 2015 due to forest management such as clear cuts, regrowth (sapling stands). In addition, we removed 10 field plots that were in too close proximity (within 10 m) to roads or water bodies. In total, we used 250 field plots for our forest floor BRF analysis with moderately rich field plots dominating and dry upland being the least represented (Table 1).

Moderately-rich sites have an abundance of herbs, grasses, and a raw hummus layer covering the ground. This fertility class grows a mix of birch, spruce, and pine. Moist upland sites are covered with feather mosses and dwarf shrubs with a spruce-dominated mixed overstory. Dryish upland sites are characterized by thick humus layer, feather mosses, cowberry and lichens. Dry upland is covered by lichen and dwarf shrubs such as heather and herbs, and few grass species. Both dryish upland and dry upland sites are typical pine habitats.

2.4. Forest floor spectral data

We used the spectral forest floor BRF measurements by Rautiainen et al. (2011) for four forest plots in Hyytiälä, Finland between 29.6.2010 and 9.7.2010. They measured four study sites representing different forest fertility site types. At each site, under diffuse light conditions, they measured forest floor spectra using a Fieldspec Handheld spectroradiometer (ASD Inc., Colorado, USA; range 325–1075 nm, 3.5 nm spectral resolution) along a 28 m transect. The selection included plots representing the four fertility sites used also in this study: moderately-rich upland (called herb-rich by Rautiainen et al. (2011), moist upland (mesic), dryish upland (sub-xeric) and dry upland (xeric) with overstory species characteristic to each fertility type.

2.5. Linear spectral unmixing

We can express the total reflectance of an image pixel as a linear combination of the component materials:

$$\mathrm{BRF} = \sum_n a_n f_n, \tag{1}$$

where a_n is the apparent BRF of the component n and f_n the corresponding weight, i.e., the proportion of each component in the instantaneous field of view (IFOV) of the sensor. Apparent reflectance (a_n) is the ratio of upwelling radiance in the field of view of the sensor to the downwelling irradiance at the top of canopy surface multiplied by the BRDF of a non-absorbing Lambertian surface. In remote sensing of vegetation, the imaginary surface for which the radiometric and reflectance quantities are given is called the top of canopy (TOC) surface. Generally, the spectral irradiance on a material inside a pixel is different from that at TOC, e.g. due to nonzero inclination angle, shading by other materials, self-shading or multiple scattering within the pixel. Therefore, the apparent reflectance a_n in Eq. (1) differs from the true spectral reflectance $r(\lambda)$ (Takala and Mõttus, 2016). The true reflectance can be calculated from apparent reflectance $a(\lambda)$ if the spectral irradiances on the material inside the pixel, $\phi(\lambda)$, and TOC, $F(\lambda)$, are known (Mõttus et al., 2015):

$$a(\lambda) = r(\lambda)\frac{\phi(\lambda)}{F(\lambda)} = r(\lambda)k(\lambda), \tag{2}$$

where $k(\lambda) = \frac{\phi(\lambda)}{F(\lambda)}$ is the reflectance conversion factor and λ is the wavelength. Thus, we can rewrite Eq.(1) as:

$$\mathrm{BRF} = \sum_n r_n k_n f_n. \tag{3}$$

With remote sensing of vegetation it is common to assume that a pixel is made up of two different materials, overstory and understory (or soil, referred here to generally as forest floor), and two different illumination conditions, sunlit and shaded (Li and Strahler, 1985). We will use the assumption that the true reflectance of shaded and sunlit canopy components are equal. Similarly, we will assume that there is no difference between the shaded and sunlit forest floor true reflectance. Hence, we arrive at:

$$\mathrm{BRF} = r_C(\lambda)[k_{C,sl}(\lambda)f_{C,sl} + k_{C,sh}(\lambda)f_{C,sh}] + r_F(\lambda)[k_{F,sl}(\lambda)f_{F,sl} + k_{F,sh}(\lambda)f_{F,sh}], \tag{4}$$

where r is the true reflectance, and the indices C, F, sl and sh indicate canopy, forest floor, sunlit component and shaded component,

Table 1
Distribution of field plots according to their fertility class.

Fertility class	Moderately-rich upland	Moist upland	Dryish upland	Dry upland	Total
Number of plots	28	177	33	12	250
Proportion in %	11	71	13	5	100

respectively.

The goal of the work presented in this paper is to calculate true understory reflectance $r_F(\lambda)$ from Eq. (4). To achieve this, we first need to determine the true reflectance of the canopy elements, $r_C(\lambda)$, and the eight model parameters: four reflectance conversion factors $k(\lambda)$ and four proportions f.

2.5.1. Spectral invariants

We applied the theory of spectral invariants to specify the reflectance of a canopy element, $r_C(\lambda)$, and to retrieve the conversion factors $k(\lambda)$. According to this theory, reflectance of a vegetation canopy in the 710–790 nm spectral interval follows the relationship:

$$\frac{\mathrm{BRF}(\lambda)}{\omega(\lambda)} = p\mathrm{BRF}(\lambda) + \rho, \tag{5}$$

where $\omega(\lambda)$ is the leaf spectral albedo, and p and ρ are spectrally invariant parameters. The spectral invariant parameters represent the slope (p) and intercept (ρ) of a linear fit between the $\omega(\lambda)$, and BRF(λ) between 710 and 790 nm. The slope is proportional to the eigenvalue of the scattering operator (Knyazikhin et al., 2013). We followed the example of Hernández-Clemente et al. (2016) and expressed BRF as a function of leaf albedo, and the irradiances on leaf and TOC:

$$\mathrm{BRF}(\lambda) = \omega(\lambda)\frac{\phi(\lambda)}{F(\lambda)}. \tag{6}$$

Next, we split the leaf irradiance $\phi(\lambda)$ into two components, an unscattered irradiance coming from the sun and sky, $\phi_S(\lambda)$, and a multiply scattered diffuse component which has at least once interacted with a canopy element or forest floor, $\phi_M(\lambda)$. We obtained from Eq. (6):

$$\frac{\mathrm{BRF}(\lambda)}{\omega(\lambda)} = \frac{\phi_M(\lambda)}{F(\lambda)} + \frac{\phi_S(\lambda)}{F(\lambda)}. \tag{7}$$

Very little angular information is available for conifers needles as its determination requires intricate vegetation measurements at different structural levels (shoot, branch, tree) and a reconstruction of tree structure. Barclay (2001) found that needle angle distributions can be close to spherical for some Northern American species, with dominantly horizontal needles for others. Niinemets et al. (2002) inverted a shoot radiative transfer model for Scots pine in Estonia to find out that its needle inclination angles are spherically distributed. For broadleaves, more information is available: Pisek et al. (2013) demonstrated birch leaves to be planophile with leaf angles determined by the shade tolerance of the species and light conditions within the canopy (Niinemets, 2010). Hence, we assumed the leaf orientation in this study area, dominated with coniferous trees, to be spherical.

For spherically oriented leaves and ignoring the contribution of diffuse sky irradiance (which is a reasonable assumption in the 710–790 nm spectral interval), Hernández-Clemente et al. (2016) obtained

$$\phi_{C,S}(\lambda) = \frac{F(\lambda)}{4\cos\theta_0}, \tag{8}$$

where θ_0 is the solar zenith angle and $F(\lambda)$ is the direct solar irradiance on a horizontal surface. For a horizontal surface, such as the forest floor, we can naturally write

$$\phi_{F,S}(\lambda) = F(\lambda).$$

Therefore, as $\phi_S(\lambda)$ is proportional to $F(\lambda)$, the second term on the right hand side of Eq. (7) is independent of the wavelength λ and equals the spectral invariant ρ in Eq. (5). The first term on the right hand side of Eq. (7) hence equals the product pBRF in Eq. (5) which allows us to write:

$$\phi_M(\lambda) = p\mathrm{BRF}(\lambda) \times F(\lambda). \tag{9}$$

Additionally, Hernández-Clemente et al. (2016) demonstrated that if the angular distribution of leaves is assumed to be spherical, the sunlit fraction of vegetation in a pixel is:

$$\alpha_{sl} = 4\rho\cos\theta_0. \tag{10}$$

Note that the derivations above are identical to those presented by Hernández-Clemente et al. (2016). We repeated them to retrieve the expression for ϕ_M (Eq. (9)) which was not explicitly given by Hernández-Clemente et al. (2016).

2.5.2. Choosing the leaf albedo

There is no absolute rule for the selection of the leaf albedo $\omega(\lambda)$. Instead, the albedo used in Eq. (5) can be scaled to represent any structural level of the canopy (Lewis and Disney, 2007; Stenberg et al., 2014). Naturally, different leaf albedos yield different values for p and ρ. An example of this scaling is the possibility to use either a needle or a shoot as the basic scattering element in a coniferous canopy. The spectral albedos of a shoot and a needle are different (but connected via the within-shoot recollision probability, Rautiainen et al., 2012), as are the recollision probabilities and fractions of sunlit elements. Proper scaling between the two structural levels guarantees that the predicted scattering BRF(λ) is the same for two approaches (Smolander and Stenberg, 2005).

The selection of structural level affects the division of reflected radiation into first-order and diffuse components making the retrieved forest floor reflectance depend somewhat on the selected leaf albedo. The p-theory assumes that the scattered radiation field inside the canopy is completely diffuse. It would therefore be most reasonable to use the albedo of a structural level, which is best related to the radiation regime below the canopy.

Rautiainen et al. (2009) have found that in boreal forests, the apparent clumping index as determined from LAI-2000 plant canopy is a unique function of the effective LAI (L_{eff}), independent of species. The apparent clumping index here refers to the value not corrected for shoot-level clumping in conifers, which is invisible to the LAI-2000. According to Rautiainen et al. (2009) apparent clumping index increases from close to 0.6 at $L_{eff} = 2$ to approximately 0.75 at $L_{eff} \simeq 4$, the largest measured L_{eff}. Hence, a value of $p_{eff} = 0.65$ is a suitable average value quantifying most forests in the study area. Mathematically, we need to find the leaf albedo ω_{eff} that would produce a recollision probability of p_{eff} when inserted into Eq. (5), while the albedos of different structural scales are connected via partial recollision probabilities p_{rel} as:

$$\omega_{eff}(\lambda) = \frac{(1 - p_{rel})\omega(\lambda)}{1 - p_{rel}\omega(\lambda)}. \tag{11}$$

After some derivations, we obtain that

$$p_{rel} = \frac{p - p_{eff}}{1 - p_{eff}}, \tag{12}$$

where p is the p-value obtained with the leaf albedo $\omega(\lambda)$.

Knyazikhin et al. (2013) have suggested the use of a PROSPECT-derived reference leaf albedo, $\omega_{ref}(\lambda)$, as the leaf albedo, $\omega(\lambda)$, which makes the model insensitive to tree species. We denote the p-value retrieved by fitting Eq. (5) to the measured BRF and $\omega_{ref}(\lambda)$ in the spectral interval of 710 to 790 nm as p_{eff}. Starting from these baseline values, we calculated the value of $r_C(\lambda)$ to be used in the linear unmixing as follows.

1. We calculated the average p-value for all 250 stands using Eq. (5) and the reference albedo ω_{ref}, $\overline{p_{ref}} = 0.81$.
2. We scaled the reference albedo to the structural level which determines canopy transmittance. We calculated p_{rel} from Eq. (12) using $\overline{p_{ref}} = 0.81$ as p, and $p_{eff} = 0.65$. We then calculated the effective leaf albedo $\omega_{eff}(\lambda)$ in the 710–790 nm spectral interval from Eq. (11).
3. The reference albedo is only applicable between 710 and 790 nm

and excludes the effects of non-green canopy material. We calculated an effective albedo of canopy scattering elements, $r_C(\lambda)$, applicable across the spectral range used in the study by assuming that the brightest pixels in the NIR (at 787 nm) represent pure overstory vegetation. Note that the brightest pixels do not necessary belong to the most reflective surfaces as brightness is the product of reflectance and irradiance; highly reflective forest floor is mostly shaded by the overstory and hence the latter is expected to dominate the brightest pixels in NIR. We fitted Eq. (5) to the mean BRF of the brightest 10% pixels [$BRF_B(\lambda)$] and $\omega_{eff}(\lambda)$ in the 710–790 nm spectral range to obtain the coefficients p_B and ρ_B for each field plot. Finally, we calculated the true effective leaf albedo $r_C(\lambda)$ for spectral unmixing as:

$$r_C(\lambda) = \frac{BRF_B(\lambda)}{p_B BRF_B(\lambda) + \rho_B}. \quad (13)$$

2.5.3. Reflectance conversion factors

To calculate the reflectance conversion factor $k_{C,\,sh}$, we made the natural assumption that shaded foliage is illuminated by multiply scattered irradiance only:

$$k_{C,sh}(\lambda) = \frac{\phi_M(\lambda)}{F(\lambda)} = p_{eff}\,BRF(\lambda). \quad (14)$$

Eq. (14) indicates that the scattered radiation field in the canopy is spectrally similar and proportional to reflectance as reflectance is a special case of scattered field: it's upward scattering at the upper canopy boundary. A similar equation can be obtained for forest floor based on Eq. (9). However, the (re)collision probability for diffuse flux traveling downwards directly above the forest floor equals unity, i.e., forest floor is treated as a solid surface and not as a turbid medium. We hence get from Eq. (14) the irradiance conversion ratio:

$$k_{F,sh}(\lambda) = BRF(\lambda). \quad (15)$$

Sunlit foliage and forest floor are additionally illuminated by the unscattered irradiance:

$$k_{C,sl}(\lambda) = \frac{\phi_M(\lambda) + \phi_{C,S}}{F(\lambda)} = p_{eff}\,BRF(\lambda) + \frac{1}{4\cos\theta_0}, \quad (16)$$

$$k_{F,sl}(\lambda) = BRF(\lambda) + 1. \quad (17)$$

Eqs. (14)–(17) allow us to retrieve all the conversion factors in Eq. (4) from remotely sensed data. Note that the spectral variation of the factors depends only on that of the canopy BRF.

2.5.4. Component proportions in a pixel

The fraction of forest floor in a pixel equals the canopy gap fraction in the view direction, $f_F = t_V$; the fraction of sunlit forest floor equals the canopy gap fraction in the solar direction, t_0. Assuming the probability for forest floor to be visible is independent of the probability for it to be sunlit, we can write:

$$f_{F,sl} = t_0 t_V. \quad (18)$$

The shaded forest floor component can be expressed as:

$$f_{F,sh} = f_F - f_{F,sl} = t_V(1 - t_0). \quad (19)$$

The spectral invariant theory allows us to retrieve the total sunlit fraction of green foliage in the IFOV, α_{sl}, using Eq. (10). In the case of a non-green forest floor, all sunlit foliage is contributed by the overstory (forest canopy). In the case of a non-vegetated background, we can thus write:

$$f_{C,sl} = \frac{\alpha_{sl}}{1 - t_V}. \quad (20)$$

In the other extreme case of a fully vegetated forest floor, the sunlit fraction of the visible foliage in a pixel, a_{sl}, is a sum of sunlit fraction of visible overstory and forest floor (assuming identical orientations of over- and understory foliage elements):

$$a_{sl} = f_{C,sl} + f_{F,sl}. \quad (21)$$

We obtain from Eqs. (18) and (21):

$$f_{C,sl} = \alpha_{sl} - t_0 t_V. \quad (22)$$

We assume that all 250 field plots have green forest floor during the time of the airborne campaign in the summer season. Hence, we used Eq. (22) to calculate total sunlit canopy fraction to account for contribution of visible understory vegetation to overstory. Finally, the fraction of shaded canopy $f_{C,\,sh}$ was calculated so that:

$$f_{C,sh} + f_{C,sl} + f_{F,sl} + f_{F,sh} = 1. \quad (23)$$

2.5.5. Canopy gap fraction estimation

We estimated the canopy gap fractions t_0 and t_V using a beta regression model reported to provide accurate results in the Finnish boreal region (Hadi et al., 2016). Unfortunately, the specific model was not available from literature and we needed to re-calibrate it. To achieve this, we used LAI-2000 canopy gap fraction measurements at five zenith angles (7°, 23°, 38°, 53°, 68°). We used the value for the first ring (7°) as t_V and interpolated linearly the canopy gap fraction measurements to the actual solar zenith angle θ_0 to obtain t_0. To find the best spectral band for our canopy gap fraction prediction we fitted a line between BRF(λ) and canopy gap fraction (t_V) for each plot and calculated the R^2 to quantify goodness of fit. Then, for each plot we fitted a linear model with BRF at 621 nm [BRF(621)], the spectral invariant p, and the sunlit fraction (α_{sl}) as the explanatory variables. Computations were made using the betareg function in R.

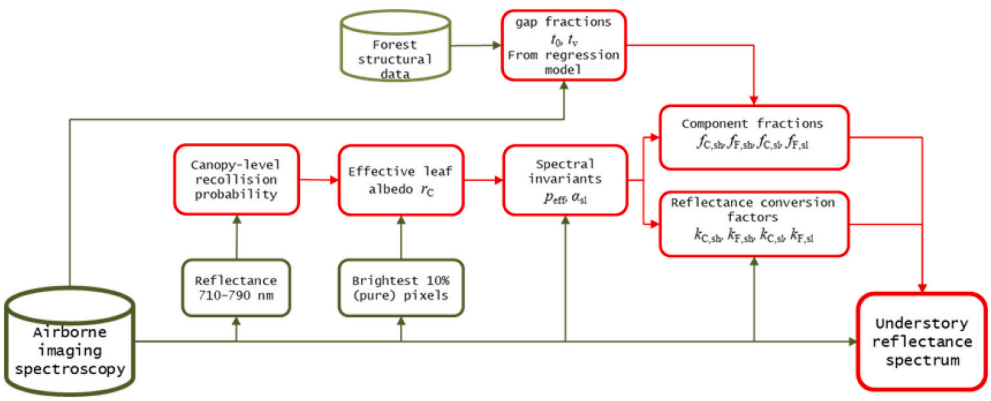

Fig. 1. Flow chart of the computations to retrieve forest floor reflectance spectrum from imaging spectroscopy data using spectral invariants and nonlinear unmixing.

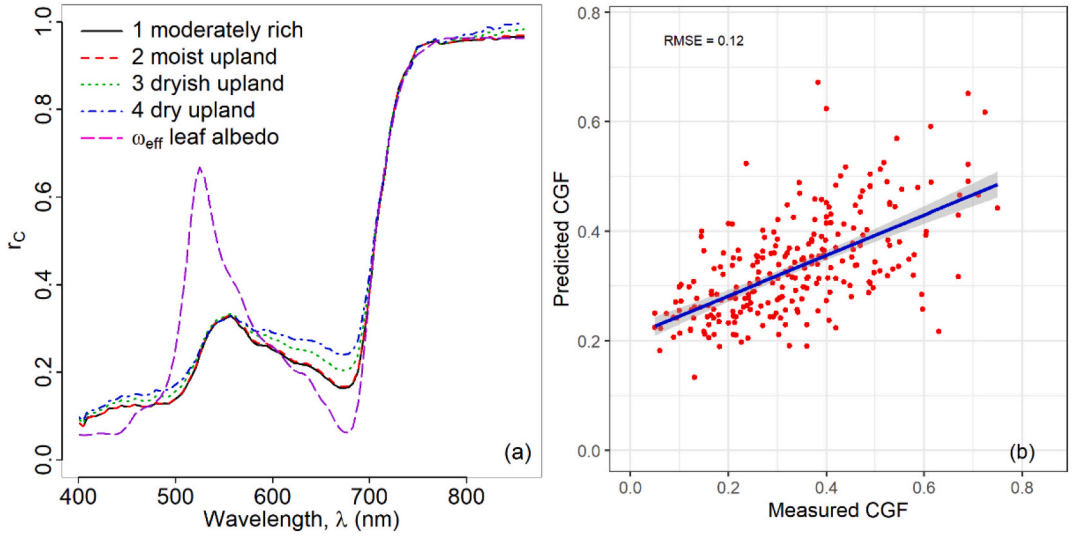

Fig. 2. a) Leaf spectra r_C for each fertility class and the PROSPECT-derived reference albedo $\omega_{eff}(\lambda)$; b) Predicted canopy gap fraction (CGF) in nadir against the value measured at 7° zenith angle with a fitted linear regression line.

2.5.6. Order of calculations

After calculating $r_C(\lambda)$ from Eq. (13) and the gap fractions as described in the above section, we determined all the forest floor and canopy fractions f in Eq. (4): the visible sunlit forest floor fraction, $f_{F,\,sl}$, from Eq. (18); the shaded forest floor fraction, $f_{F,\,sh}$, from Eq. (19); the sunlit canopy fraction, $f_{C,\,sl}$, from Eq. (22); and the shaded canopy fraction, $f_{C,\,sh}$, from Eq. (23). Finally, we calculated the canopy and forest floor reflectance conversion factors k: the shaded canopy factor, $k_{C,\,sh}$, from Eq. (14); the sunlit canopy factor, $k_{C,\,sl}$, from Eq. (16); the sunlit forest floor factor, $k_{F,\,sl}$, from Eq. (17); and the shaded forest floor

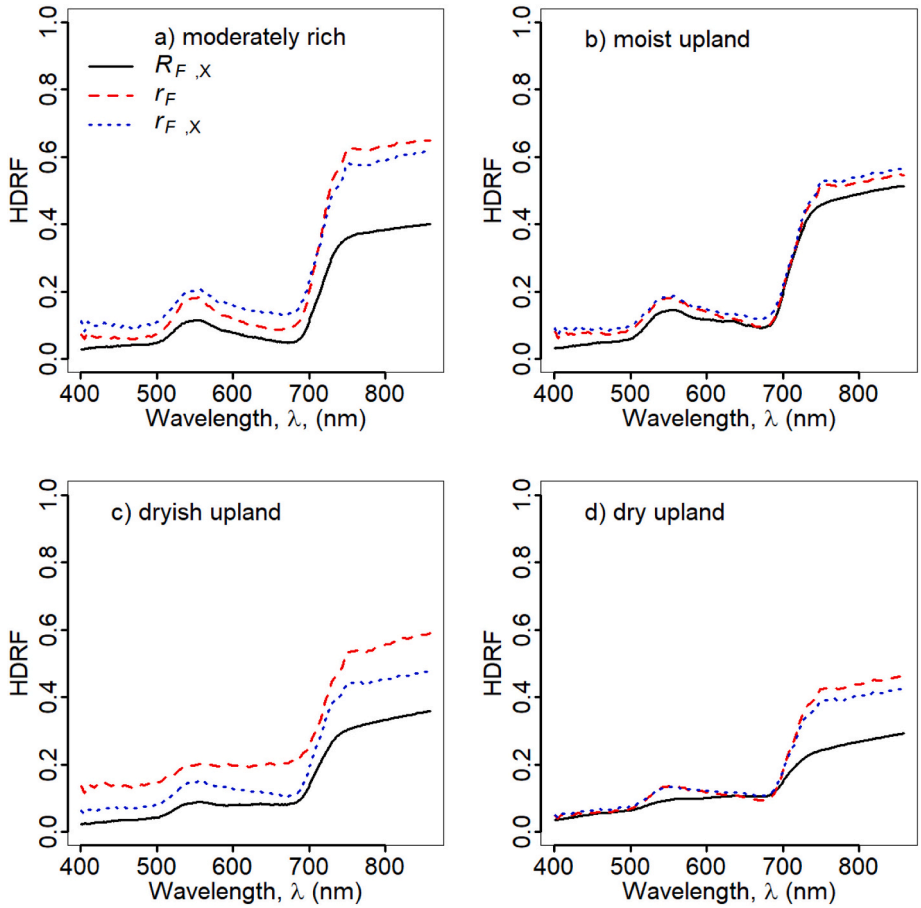

Fig. 3. The measured forest floor reflectance, $R_{F,\,X}(\lambda)$, (black line), $r_F(\lambda)$ for the same single plot (red dotted line), and the fertility class average $\overline{r_{F,X}(\lambda)}$ (blue dotted line) for a) moderately-rich (herb-rich), b) moist upland (mesic), c) dryish upland (sub-xeric), and d) dry upland (xeric) plots. The site fertility types given in parentheses are the ones used by Rautiainen et al. (2011) who provided the field-measured spectra. (For interpretation of the references to colour in this figure legend, the reader is referred to the web version of this article.)

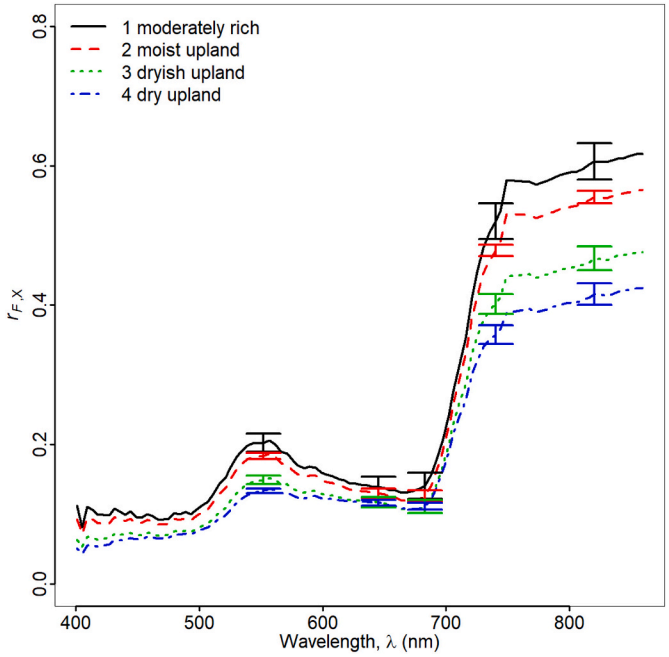

Fig. 4. The average forest floor reflectance for four fertility classes as retrieved from AHS, $\overline{r_{F,X}(\lambda)}$, with 95% confidence intervals plotted at 552, 645,683, 739 and 820 nm.

Table 2
Significance of $\overline{r_{F,X}(\lambda)}$ differences among all fertility class combinations at 552 nm (upper-right part of table) and 820 nm (bottom-left part). The *P*-values significance codes are indicated with * ($P < 0.01$), ** ($P < 0.05$),— ($P > 0.05$).

	Moderately-rich	Moist upland	Dryish upland	Dry upland
Moderately-rich		–	*	*
Moist upland	*		*	*
Dryish upland	*	*		*
Dry upland	*	*	*	

factor, $k_{F,\,sh}$, from Eq. (15). Knowing all eight model parameters and $r_C(\lambda)$, we could solve Eq. (4) for $r_F(\lambda)$. A flow chart of the processing steps is given in Fig. 1.

2.5.7. Forest floor BRF as a function of site fertility

Forest floor reflectance and site fertility are both directly connected to the amount and composition of understory. To determine whether the mean $r_F(\lambda)$ for each fertility class *X*, $\overline{r_{F,X}(\lambda)}$, is statistically significantly different from one another we performed pairwise comparisons. We used two-tailed Welch's *t*-tests in *R* (function name: "t.test" with arguments: "two.sided") to find the significant differences of $\overline{r_{F,X}(\lambda)}$ between fertility classes. For each fertility class *X* we calculated the 95% confidence interval *E* of $\overline{r_{F,X}(\lambda)}$ as:

$$E = 1.96\frac{\sigma_{rU}}{\sqrt{n}}, \tag{24}$$

where σ is the standard deviation of $r_F(\lambda)$ for each fertility class, and *n* is the number of field plots belonging to this class.

2.6. Calculation of PRI

PRI is defined as (Gamon et al., 1992):

$$\mathrm{PRI} = \frac{R(531) - R(570)}{R(531) + R(570)} \tag{25}$$

where $R(\lambda)$ is the reflectance at the wavelength λ given in nanometers.

We calculated four PRI values:

1. forest PRI, by using TOC BRF as *R* in Eq. (25)
2. overstory PRI, by using $r_C(\lambda)[k_{C,\,sl}(\lambda)f_{C,\,sl} + k_{C,\,sh}(\lambda)f_{C,\,sh}]$ from Eq. (4) as *R*
3. leaf-level PRI, by using r_C as *R*;
4. understory PRI, by using r_F as *R*.

We then plotted overstory PRI, understory PRI, and leaf-level PRI each against TOC PRI evaluated their correlation using the Pearson's correlation coefficient and the *t*-test to determine the statistical significance of the correlation.

3. Results

3.1. Leaf spectra and canopy gap fraction

As expected, the canopy leaf spectra r_C from Eq. (13) and the PROSPECT-derived reference albedo ω_{eff} were identical between 710 and 790 nm. The r_C averaged over each site fertility class was higher than ω_{eff} in the blue and red regions (Fig. 2a) and close to ω_{eff} in the green (550 nm) and red edge (720 nm) regions.

The predicted canopy gap fractions (t_0 and t_V), used in Eq. (22) to estimate $f_{C,\,sl}$, had a linear correlation with the field-measured values. The coefficient of determination (R^2) was 0.37 and RMSE = 0.12 (Fig. 2b).

3.2. Forest floor reflectance

In general, the magnitude of $\overline{r_{F,X}(\lambda)}$ was overestimated for all four field plots compared to that obtained from field measurements, $R_{F,\,X}(\lambda)$, where *X* is the fertility class (Fig. 3). This is especially visible in the green (550 nm) region and the NIR (700–900 nm). The opposite happened for moist upland (mesic) and dry upland (xeric) plots in the red region at 700 nm. Similarly, the overestimation in green and NIR occurred for $R_{F,\,X}(\lambda)$ for each of the four studied fertility classes. What is noteworthy is the difference between $R_{F,\,X}(\lambda)$ and $\overline{r_{F,X}(\lambda)}$ for dryish upland (Fig. 3c). Whereas, moist upland had less disparity between $R_{F,\,X}(\lambda)$ and $\overline{r_{F,X}(\lambda)}$.

The forest floor field spectra (black lines in Fig. 3) and all AHS-derived r_U spectra (Fig. 4) demonstrated typical green vegetation spectra with strong absorption in red and large reflectance in the NIR region. This supports our assumption to use green forest floor in Eq. (22). The $\overline{r_{F,X}(\lambda)}$ of different fertility classes became visibly separable in the green region, around 550 nm, and even more so in the NIR region (Fig. 4). In the latter we observed the largest spectral differences in r_U between the fertility classes. In addition, $\overline{r_{F,X}(\lambda)}$ in the NIR region increased with site fertility while it was approximately the same for all fertility classes (Fig. 4) in the red region (680 nm). Despite the overlap in the green region at 552 nm (Fig. 4), the differences were statistically significant) between moderately-rich and moist upland (Table 2), and for all other pairs, the was highly significantly different. Even though the variation ranges of understory spectra for the different fertility classes overlapped in the red (683 nm), *t*-tests showed a significant difference ($P < 0.01$) $\overline{r_{F,X}(\lambda)}$ between moderately rich and dryish upland, and moderately rich and dry upland. Moist upland $\overline{r_{F,X}(\lambda)}$ is significantly different ($P < 0.05$) from dryish upland, and dry upland ($P < 0.01$). We observed the largest differences in $\overline{r_{F,X}(\lambda)}$ in the NIR region between the fertility classes, where *t*-tests (Table 2) showed significant differences ($P < 0.01$) between all four studied fertility classes.

3.3. Leaf, understory and canopy PRI

The TOC BRF PRI correlations with overstory PRI ($r^2 = -0.0038$), r_C PRI ($r^2 = -0.004$), and r_F($r^2 = -0.003$ were very weak but

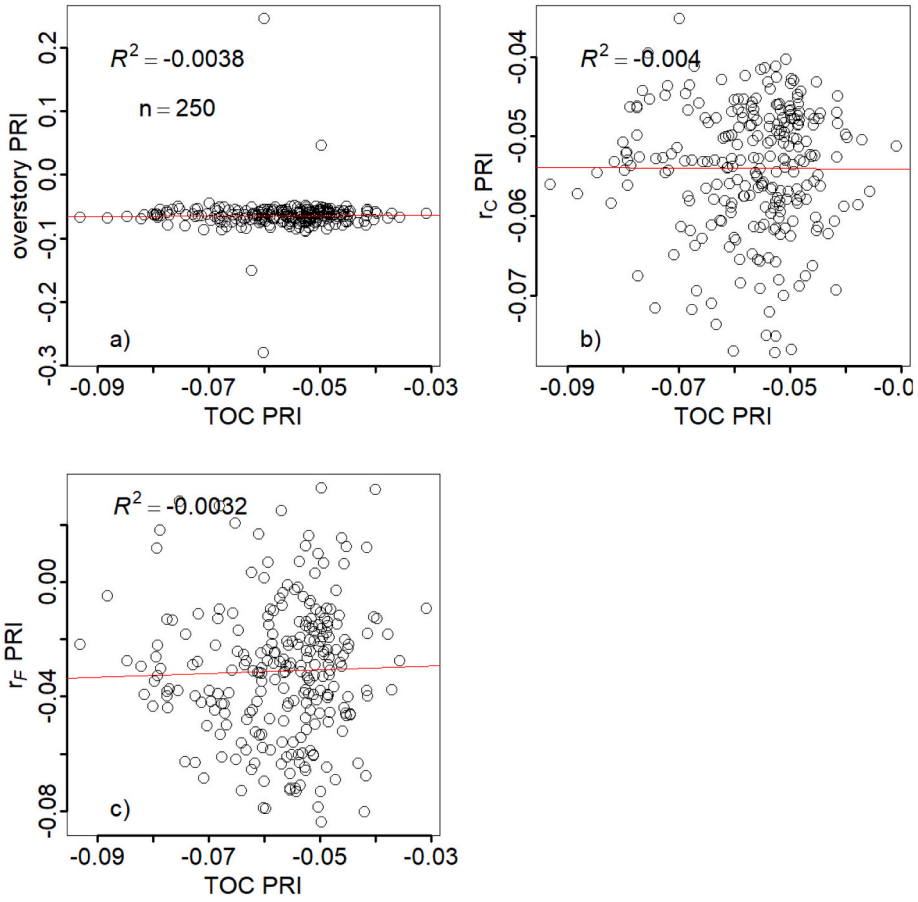

Fig. 5. a) Overstory PRI, b) $r_C PRI$, and c) r_F PRI as functions of TOC PRI for 250 field plots.

statistically significant $P < 0.01$, $P < 0.01$, $P < 0.01$, respectively (Fig. 5). The smallest mean PRI value of −0.09 was measured for overstory;r_F, r_C and TOC BRF produced PRI of −0.064, −0.068, and −0.056, respectively. The TOC PRI was statistically different from the three other PRI values ($P < 0.01$).

4. Discussion

The observed variation in $r_F(\lambda)$ spectra within each site fertility class (Fig. 4) could be caused by the normal variation in understory vegetation composition, or forest management practices, such as stand thinning, which can damage the understory or cover it with cutting residues. Nevertheless, the general trends agree with the general understanding that herb-moderately rich understory vegetation, indicative of rich abundance of nutrients, is characterized by mosses and large distribution of herbs, grasses and ferns agreeing with the higher NIR reflectance compared to other fertility sites. In contrast, dryish and dry uplands lack the nutrient richness and the ground cover is dominated by lichen and dwarf shrubs, leading to a lower NIR reflectance (Rantala et al., 2011).

The $\overline{r_{F,X}(\lambda)}$ spectra show a pattern similar to the measured forest floor spectra, originally reported by Rautiainen et al. (2011; their fig. 3C), with moist upland (mesic) having the highest reflectance up to 0.15 HDRF in the green region (550 nm), and up to 0.52 HDRF in the NIR region (850 nm). Moreover, their results show that dry upland (xeric) is the least reflective fertility class in green and NIR but compared to the other fertility classes is most sensitive in the red region. In general, however, the reported forest floor HDRF for dry upland had approximately 30% lower reflectance in the NIR region. These results agree with our results in Fig. 4 where $\overline{r_{F,X}(\lambda)}$ spectra increases in the green and NIR spectral region as fertility class increases. Their results differ from our results in the red region around 680 nm, where they have a larger variation, up to 0.07, in $\overline{r_{F,X}(\lambda)}$ among fertility classes compared to our 0.01. In general, our $r_U(\lambda)$ is approximately 20% higher in green and NIR. We hypothesize that this is due to the use of the reference albedo which ignores non-green material, leading to an inaccurate $r_C(\lambda)$ in Eq. (4), and hence inaccurate unmixing of reflectance.

The understory retrieval algorithm requires specification whether the forest floor is green or not, and choosing the appropriate equation, (21) or (22). We only tested it using forests in Finland where no soil is visible and, during growing season, forest floor has a clear red edge indicative of green vegetation (Rautiainen et al., 2011). Moreover, the algorithm likely fail during the end or beginning of the growing season when the forest floor is covered with snow. We understand the spatial and temporal limitations of our proposed algorithm and a more robust version of our algorithm needs to be developed for different forest types.

For reliable understory HDRF, the understory signal should be strongly present in forest BRF, which does not hold for very closed canopies. The algorithm will fail for very closed as well as open canopies. However, the algorithm assumes substantial overstory cover (by assuming that the 10% brightest pixels in NIR are dominated by overstory signal) and is hence likely to fail for open canopy woodlands.

The study done by Kuusinen et al. (2015) also produced $\overline{r_{F,X}(\lambda)}$ results similar to ours. They used linear spectral unmixing and Landsat spectral data to calculate sunlit forest floor BRF by site fertility and tree species for a boreal forest in Finland. Their results showed an increase in sunlit forest floor reflectance in NIR (760–900 nm) with increasing site fertility, from 0.18 for least fertile to 0.32 BRF at the most fertile site. Moreover, they observed a slight increase in forest floor BRF in the red (630–690 nm) region as fertility site increases. These results agree

with our $\overline{r_{F,X}(\lambda)}$ spectra presented in Fig. 4 that show a similar pattern with a slight increase in forest floor BRF in the red region. Their model required information on canopy gap fraction measurements, tree species information, and site fertility to be solvable, whereas our model is independent of species information and retrieves gap fractions from spectral reflectance data.

Lastly, a similar study by Pisek et al. (2010) in which they used airborne hyperspectral imagery to estimate forest floor BRF for a Canadian coniferous forest reported results between 0.04 and 0.06 in the red spectral region (671 nm). These results are slightly lower compared to our $\overline{r_{F,X}(671)} \simeq 0.1$. Additionally, they reported forest floor BRFs between 0.3 and 0.5 in the NIR spectral band (866 nm) which is a similar range to our 0.4 to 0.6 range. While, these results are similar to ours, our study results are only representative for European boreal forests.

Estimating forest floor BRF requires knowledge of the leaf albedo and the canopy gap fraction (CGF). The leaf albedo used in the study varies somewhat with species, although its value at 790 nm (and NIR in general) is determined by that of the reference albedo, ω_{ref} (Fig. 2a). The variation of $r_C(\lambda)$ with fertility class is determined by the dependence of species composition on site fertility and causes differences in retrieved leaf reflectance $r_C(\lambda)$ (which includes also the effect of non-green material) in the visible part of the spectrum. Also, the leaf angle distribution, or, more specifically, the *G*-function in the solar direction needs to be known. This value affects the estimates of the fraction of sunlit foliage and the irradiance on sunlit leaves. These lead to variations in the modeled contributions of first- and higher-order scattering to the canopy-reflected signal, and also total canopy scattering. However, our analyses using different values for *G* suggest that the uncertainty in leaf orientation translates to an r_U uncertainty smaller than 10% (relative units). The G-function is known to be species-specific and can potentially be estimated from hyperspectral data, although according to our knowledge, it has only been attempted for field crops (Zou and Mõttus, 2015).

CGF quantifies the overstory canopy structure and determines how much light penetrates through the canopy to the forest floor. A reliable CGF estimate is also the key to the robustness of the algorithm. The unmixing Eq. (4) indicates that the (estimated) canopy gap fraction largely determines the contribution of canopy to the total BRF. For small CGF values, even large relative errors in canopy contribution have a small effect (due to the small absolute contribution of the canopy). For large CGF values, even small errors in canopy reflectance contribution estimation (e.g., due to an incorrect CGF estimate) can translate to large errors in the estimate of forest floor reflectance contribution, and hence also its reflectance factor.

Measuring CGF in the field is a laborious task, especially for larger areas, hence we wanted to predict CGF from remote sensing data. As no wide-area models or products are readily available, to determine this parameter from remote sensing data, we selected a published model covering a large geographic area (Hadi et al., 2016). A more limited study has also shown that the p-theory can provide an estimate for this parameter via a linear correlation with $\ln|1-p|$ (Vanhatalo et al., 2014). Kuusinen et al. (2015) demonstrated that the forest floor contribution in the NIR to TOC BRF decreases as tree height, LAI, and canopy cover increases. This suggests an increased effect of CGF on the retrieved $r_F(\lambda)$, and a larger error in $r_F(\lambda)$ in NIR. The agreement of retrieved $r_F(\lambda)$ in the NIR region with other studies suggest our model has sufficient accuracy. To further test the robustness of the forest floor reflectance retrieval algorithm to true variations in CGF (i.e., assuming that CGF is correctly estimated), we retrieved forest floor BRF for plots with high and low LAI (low and high CGF, respectively). For the test plots, we had reliable ground-measured CGF and optical LAI data. The retrieved forest floor BRF changed little with canopy cover for each fertility class (data not shown), which indicates the robustness of the retrieval algorithm to variations in overstory cover.

According to our unmixing algorithm, the PRI value of the canopy is not correlated with that of leaves, overstory or understory across the wide variety of canopy structures used in the study. The most surprising results is a lack of correlation between TOC BRF-derived PRI and the value calculated from the leaf reflectance, r_C. The latter is directly calculated from 10% of the brightest pixels. This result demonstrates the large variation in PRI with shadow fraction for vegetation canopies, caused by multiple scattering, shading, diffuse illumination and, last and not least, possible variation of PRI with irradiation conditions. Before an in-depth analysis, these results cannot be used as direct validation of a lack of correlation between forest and leaf PRI, but nevertheless provide yet another indication of the complexity of PRI scaling.

We did not fully utilize the potential of the high spatial resolution data as we only used the high spatial resolution to select the brightest pixels. Despite the decreased signal to noise ratio in shaded pixels, the 0.6 m resolution can be utilized for forest floor retrieval if pure pixels, so called 'endmembers' can be determined from data. Two possible endmembers that are to be included are apparent reflectance of shaded and sunlit leaves (as described by Mõttus et al., 2015), and sunlit and shaded forest floor.

Previously, medium-resolution satellite data has been used in most studies of forest floor reflectance retrieval (Jiao et al., 2014; Kuusinen et al., 2015; Liu et al., 2017; Pisek et al., 2015b; Pisek and Chen, 2009; Rautiainen and Heiskanen, 2013). The algorithm presented here at plot level will, in principle, also work with a spatial resolution of 10–20 m after slight modifications. It would not be possible to use the brightest canopy leaf spectra to calculate $r_C(\lambda)$, and average canopy reflectance will need to be used; alternatively, canopy element reflectance may be determined from auxiliary data sources (e.g., spectral databases).

The linear mixture model presented in Eq. (4) is not fundamentally new and has also been used, with appropriate adaptations, in previous works (Kuusinen et al., 2015; Li and Strahler, 1985; Pisek et al., 2015a). The new aspect here is explicitly distinguishing true and apparent reflectances, and presenting forest reflectance as a function of physically measurable reflectance properties. Instead of the abstract sunlit canopy reflectance, we define forest BRF via the reflectance properties of the physical objects scattering the radiation. We believe that the use of leaf albedo, despite its variation with species and phenology, improves the robustness of the retrieval of r_F. The switch from the actual reflectance of the canopy element to the reference albedo makes the model mathematically more complex but may be necessary to account for the large diversity of green vegetation mapped by remote sensing instruments.

In this paper, we presented an algorithm that separates the contribution of apparent forest floor from apparent overstory HDRF using an airborne hyperspectral remote sensing data independent of forest stand data obtained through extensive fieldwork. This algorithm can be used to calculate apparent forest floor HDRF and apparent overstory HDRF at field plot level. Moreover, the algorithm can provide a solution to separate site fertility classes using their true forest floor HDRF. However, more work is needed to improve the retrieval of other canopy biophysical characteristics, most critically gap fractions as the algorithm described here depends on them. The retrieval of gap fractions is not only critical for quantifying the direct contribution of understory reflectance to canopy-leaving radiance, but also for determining the canopy-level recollision probability p_{eff} (Eq. 12) which determines canopy diffuse transmittance as demonstrated by (Stenberg, 2007). It is clear that in the case of a physically based algorithm, the retrieved values of vegetation state variables are interrelated. It would hence be reasonable to attempt a simultaneous retrieval of gap fraction, recollision probability, and understory reflectance, in a comprehensive reflectance parametrization of vegetation reflectance based on spectral invariants – for example, as an advanced version of the PARAS model (Rautiainen and Stenberg, 2005). Furthermore, there is no clear understand the effect of the assumption of green forest floor, and the full diversity of possible canopy structures on the retrieval result. The

algorithm needs also further validation, hopefully with field data measured simultaneously with remote sensing acquisition. Unfortunately, spatially extensive field measurements of forest floor reflectance are scarce and laborious to obtain.

5. Conclusion

We demonstrated, using a linear spectral unmixing algorithm, that we were able to separate forest floor and overstory HDRF for different fertility sites from airborne hyperspectral remote sensing imagery data without the input of field stand variables. We observed an increase in true forest floor HDRF from nutrient poor sites to nutrient rich sites in both the green (550 nm) and NIR (820 nm) regions. The promising results presented in this paper can help to create in the future operational algorithms to separate forest floor and overstory reflectance from airborne imaging spectroscopy with possible application to medium-resolution satellite data.

Declaration of Competing Interests

The authors declare that they have no known competing financial interests or personal relationships that could have appeared to influence the work reported in this paper.

Declaration of Competing Interest

None.

Acknowledgements

The authors would like to thank the Academy of Finland (grants 266152, 272989, 303633 and 317387) for providing the funds. We are grateful to Dr. Lauri Korhonen (University of Eastern Finland) and Dr. Titta Majasalmi (NIBIO) for providing the field data of the test stands, Dr. Rocío Hernández-Clemente (University of Swansea, UK) for her valuable input in the study- and concept design, and MSc Viljami Perheentupa for valuable technical assistance.

References

Adams, J.B., Smith, M.O., Johnson, P.E., 1986. Spectral mixture modeling: A new analysis of rock and soil types at the Viking Lander 1 Site. J. Geophys. Res. Solid Earth 91, 8098–8112. https://doi.org/10.1029/JB091iB08p08098.

Asner, G.P., Keller, M., Pereira, R., Zweede, J.C., Silva, J.N.M., 2004. Canopy damage and recovery after selective logging in Amazonia: Field and satellite studies. Ecol. Appl. 14, 280–298. https://doi.org/10.1890/01-6019.

Barclay, H.J., 2001. Distribution of leaf orientations in six conifer species. Can. J. Bot. 79, 389–397. https://doi.org/10.1139/b01-014.

Barton, C.V.M., North, P.R.J., 2001. Remote sensing of canopy light use efficiency using the photochemical reflectance index. Model and sensitivity analysis. Remote Sens. Environ. 78, 264–273. https://doi.org/10.1016/S0034-4257(01)00224-3.

Damm, A., Guanter, L., Verhoef, W., Schläpfer, D., Garbari, S., Schaepman, M.E., 2015. Impact of varying irradiance on vegetation indices and chlorophyll fluorescence derived from spectroscopy data. Remote Sens. Environ. 156, 202–215. https://doi.org/10.1016/j.rse.2014.09.031.

Eriksson, H.M., Eklundh, L., Kuusk, A., Nilson, T., 2006. Impact of understory vegetation on forest canopy reflectance and remotely sensed LAI estimates. Remote Sens. Environ. 103, 408–418. https://doi.org/10.1016/j.rse.2006.04.005.

Fitzgerald, G.J., Pinter Paul, J., Hunsaker, D.J., Clarke, T.R., 2004. Shadow fraction in spectral mixture analysis of a cotton canopy. pp. 20–34.

Gamon, J.A., Peñuelas, J., Field, C.B., 1992. A narrow-waveband spectral index that tracks diurnal changes in photosynthetic efficiency. Remote Sens. Environ. 41, 35–44. https://doi.org/10.1016/0034-4257(92)90059-S.

Goodwin, N., Coops, N.C., Stone, C., 2005. Assessing plantation canopy condition from airborne imagery using spectral mixture analysis and fractional abundances. Int. J. Appl. Earth Obs. Geoinf. 7, 11–28. https://doi.org/10.1016/j.jag.2004.10.003.

Hadi, K.L., Hovi, A., Rönnholm, P., Rautiainen, M., 2016. The accuracy of large-area forest canopy cover estimation using Landsat in boreal region. Int. J. Appl. Earth Obs. Geoinf. 53, 118–127. https://doi.org/10.1016/j.jag.2016.08.009.

Hallik, L., Kull, O., Nilson, T., Peñuelas, J., 2009. Spectral reflectance of multispecies herbaceous and moss canopies in the boreal forest understory and open field. Can. J. Remote. Sens. 35, 475–485. https://doi.org/10.5589/m09-040.

Heiskanen, J., Rautiainen, M., Stenberg, P., Mõttus, M., Vesanto, V.H., Korhonen, L., Majasalmi, T., 2012. Seasonal variation in MODIS LAI for a boreal forest area in Finland. Remote Sens. Environ. 126, 104–115. https://doi.org/10.1016/j.rse.2012.08.001.

Hernández-Clemente, R., Kolari, P., Porcar-Castell, A., Korhonen, L., Mõttus, M., 2016. Tracking the seasonal dynamics of boreal forest photosynthesis using EO-1 Hyperion reflectance: Sensitivity to structural and illumination effects. IEEE Trans. Geosci. Remote Sens. 54, 5105–5116. https://doi.org/10.1109/TGRS.2016.2554466.

Jiao, T., Liu, R., Liu, Y., Pisek, J., Chen, J.M., 2014. Mapping global seasonal forest background reflectivity with multi-angle imaging Spectroradiometer data. J. Geophys. Res. Biogeosci. 119, 1063–1077. https://doi.org/10.1002/2013JG002493.

Jiménez-Muñoz, J.C., Sobrino, J.A., Plaza, A., Guanter, L., Moreno, J., Martínez, P., 2009. Comparison between fractional vegetation cover retrievals from vegetation indices and spectral mixture analysis: Case study of PROBA/CHRIS data over an agricultural area. Sensors 9, 768–793. https://doi.org/10.3390/s90200768.

Knyazikhin, Y., Schull, M.A., Stenberg, P., Mõttus, M., Rautiainen, M., Yang, Y., Marshak, A., Latorre Carmona, P., Kaufmann, R.K., Lewis, P., Disney, M.I., Vanderbilt, V., Davis, A.B., Baret, F., Jacquemoud, S., Lyapustin, A., Myneni, R.B., 2013. Hyperspectral remote sensing of foliar nitrogen content. Proc. Natl. Acad. Sci. U. S. A. 110, E185–E192. https://doi.org/10.1073/pnas.1210196109.

Korhonen, L., Korpela, I., Heiskanen, J., Maltamo, M., 2011. Airborne discrete-return LIDAR data in the estimation of vertical canopy cover, angular canopy closure and leaf area index. Remote Sens. Environ. 115, 1065–1080. https://doi.org/10.1016/J.RSE.2010.12.011.

Kuusela, K., Salminen, S., 1969. The 5th national forest inventory in Finland. General design, instructions for field work and data processing. Commun. Inst. Forest. Fenn 69, 72.

Kuusinen, Nea, Stenberg, Pauline, Tomppo, Erkki, Bernier, Pierre, Berninger, Frank, Kuusinen, N., Stenberg, P., Berninger, F., Tomppo, E., Bernier, P., 2015. Variation in understory and canopy reflectance during stand development in Finnish coniferous forests. Can. J. For. Res. 45, 1077–1085. https://doi.org/10.1139/cjfr-2014-0538.

Kuusk, A., Lang, M., Nilson, T., 2004. Simulation of the reflectance of ground vegetation in sub-boreal forests. Agric. For. Meteorol. 126, 33–46. https://doi.org/10.1016/j.agrformet.2004.05.004.

Leboeuf, A., Beaudoin, A., Fournier, R.A., Guindon, L., Luther, J.E., Lambert, M.-C., 2007. A shadow fraction method for mapping biomass of northern boreal black spruce forests using QuickBird imagery. Remote Sens. Environ. 110, 488–500. https://doi.org/10.1016/j.rse.2006.05.025.

Lewis, P., Disney, M., 2007. Spectral invariants and scattering across multiple scales from within-leaf to canopy. Remote Sens. Environ. 109, 196–206. https://doi.org/10.1016/j.rse.2006.12.015.

Li, X., Strahler, A.H., 1985. Geometric-optical modeling of a conifer forest canopy. IEEE Trans. Geosci. Remote Sens. GE-23, 705–721. https://doi.org/10.1109/TGRS.1985.289389.

Liu, Y., Liu, R., Pisek, J., Chen, J.M., 2017. Separating overstory and understory leaf area indices for global needleleaf and deciduous broadleaf forests by fusion of MODIS and MISR data. Biogeosciences 14, 1093–1110. https://doi.org/10.5194/bg-14-1093-2017.

Majasalmi, T., Rautiainen, M., Stenberg, P., Rita, H., 2012. Optimizing the sampling scheme for LAI-2000 measurements in a boreal forest. Agric. For. Meteorol. 154–155, 38–43. https://doi.org/10.1016/J.AGRFORMET.2011.10.002.

Majasalmi, T., Rautiainen, M., Stenberg, P., Manninen, T., 2015. Validation of MODIS and GEOV1 fPAR products in a boreal forest site in Finland. Remote Sens. 7, 1359–1379. https://doi.org/10.3390/rs70201359.

Miller, J.R., White, H.P., Chen, J.M., Peddle, D.R., McDermid, G., Fournier, R.A., Shepherd, P., Rubinstein, I., Freemantle, J., Soffer, R., LeDrew, E., 1997. Seasonal change in understory reflectance of boreal forests and influence on canopy vegetation indices. J. Geophys. Res. Atmos. 102, 29475–29482. https://doi.org/10.1029/97JD02558.

Mõttus, M., Takala, T.L.H., Stenberg, P., Knyazikhin, Y., Yang, B., Nilson, T., 2015. Diffuse sky radiation influences the relationship between canopy PRI and shadow fraction. ISPRS J. Photogramm. Remote Sens. 105, 54–60. https://doi.org/10.1016/j.isprsjprs.2015.03.012.

NASA, 2019. AERONET: Aerosol Robotic Network. [WWW Document]. URL. https://aeronet.gsfc.nasa.gov/ (accessed 2.18.19).

Niinemets, Ü., 2010. A review of light interception in plant stands from leaf to canopy in different plant functional types and in species with varying shade tolerance. Ecol. Res. 25, 693–714. https://doi.org/10.1007/s11284-010-0712-4.

Niinemets, Ü., Cescatti, A., Lukjanova, A., Tobias, M., Truus, L., 2002. Modification of light-acclimation of *Pinus sylvestris* shoot architecture by site fertility. Agric. For. Meteorol. 111, 121–140. https://doi.org/10.1016/S0168-1923(02)00011-4.

Peddle, D.R., Hall, F.G., LeDrew, E.F., 1999. Spectral mixture analysis and geometric-optical reflectance modeling of boreal forest biophysical structure. Remote Sens. Environ. 67, 288–297. https://doi.org/10.1016/S0034-4257(98)00090-X.

Peltoniemi, J.I., Kaasalainen, S., Näränen, J., Rautiainen, M., Stenberg, P., Smolander, H., Smolander, S., Voipio, P., 2005. BRDF measurement of understory vegetation in pine forests: Dwarf shrubs, lichen, and moss. Remote Sens. Environ. 94, 343–354. https://doi.org/10.1016/j.rse.2004.10.009.

Pisek, J., Chen, J.M., 2009. Mapping forest background reflectivity over North America with Multi-angle Imaging SpectroRadiometer (MISR) data. Remote Sens. Environ. 113, 2412–2423. https://doi.org/10.1016/j.rse.2009.07.003.

Pisek, J., Chen, J.M., Miller, J.R., Freemantle, J.R., Peltoniemi, J.I., Simic, A., 2010. Mapping forest background reflectance in a boreal region using multiangle compact airborne spectrographic imager data. IEEE Trans. Geosci. Remote Sens. 48, 499–510. https://doi.org/10.1109/TGRS.2009.2024756.

Pisek, J., Rautiainen, M., Heiskanen, J., Mõttus, M., 2012. Retrieval of seasonal dynamics of forest understory reflectance in a northern European boreal forest from MODIS

BRDF data. Remote Sens. Environ. 117, 464–468. https://doi.org/10.1016/j.rse.2011.09.012.
Pisek, J., Sonnentag, O., Richardson, A.D., Mõttus, M., 2013. Is the spherical leaf inclination angle distribution a valid assumption for temperate and boreal broadleaf tree species? Agric. For. Meteorol. 169, 186–194. https://doi.org/10.1016/j.agrformet.2012.10.011.
Pisek, J., Lang, M., Kuusk, J., 2015a. A note on suitable viewing configuration for retrieval of forest understory reflectance from multi-angle remote sensing data. Remote Sens. Environ. 156, 242–246. https://doi.org/10.1016/j.rse.2014.09.033.
Pisek, J., Rautiainen, M., Nikopensius, M., Raabe, K., 2015b. Estimation of seasonal dynamics of understory NDVI in northern forests using MODIS BRDF data: Semi-empirical versus physically-based approach. Remote Sens. Environ. 163, 42–47. https://doi.org/10.1016/J.RSE.2015.03.003.
Rantala, S., Tammiruussu, P., Erkki, S., 2011. Finnish Forestry Practice and Management. Metsäkustannus, Helsinki.
Rautiainen, M., Heiskanen, J., 2013. Seasonal contribution of understory vegetation to the reflectance of a boreal landscape at different spatial scales. IEEE Geosci. Remote Sens. Lett. 10, 923–927. https://doi.org/10.1109/LGRS.2013.2247560.
Rautiainen, M., Stenberg, P., 2005. Application of photon recollision probability in coniferous canopy reflectance simulations. Remote Sens. Environ. 96, 98–107. https://doi.org/10.1016/J.RSE.2005.02.009.
Rautiainen, M., Mõttus, M., Stenberg, P., 2009. On the relationship of canopy LAI and photon recollision probability in boreal forests. Remote Sens. Environ. 113, 458–461. https://doi.org/10.1016/j.rse.2008.10.014.
Rautiainen, M., Mõttus, M., Heiskanen, J., Akujärvi, A., Majasalmi, T., Stenberg, P., 2011. Seasonal reflectance dynamics of common understory types in a northern European boreal forest. Remote Sens. Environ. 115, 3020–3028. https://doi.org/10.1016/j.rse.2011.06.005.
Rautiainen, M., Mõttus, M., Yáñez-Rausell, L., Homolová, L., Malenovský, Z., Schaepman, M.E., 2012. A note on upscaling coniferous needle spectra to shoot spectral albedo. Remote Sens. Environ. https://doi.org/10.1016/j.rse.2011.10.019.
Rees, W.G., Tutubalina, O.V., Golubeva, E.I., 2004. Reflectance spectra of subarctic lichens between 400 and 2400 nm. Remote Sens. Environ. https://doi.org/10.1016/j.rse.2003.12.009.
Rogan, J., Miller, J., 2006. Integrating GIS and remotely sensed data for mapping forest disturbance and change. Underst. For. Disturb. Spat. Pattern Remote Sens. GIS Approaches 133–170.
Schaepman-Strub, G., Limpens, J., Menken, M., Bartholomeus, H.M., Schaepman, M.E., 2009. Towards spatial assessment of carbon sequestration in peatlands: Spectroscopy based estimation of fractional cover of three plant functional types. Biogeosciences. https://doi.org/10.5194/bg-6-275-2009.
Smolander, S., Stenberg, P., 2005. Simple parameterizations of the radiation budget of uniform broadleaved and coniferous canopies. Remote Sens. Environ. 94, 355–363. https://doi.org/10.1016/j.rse.2004.10.010.
Somers, B., Asner, G.P., Tits, L., Coppin, P., 2011. Endmember variability in spectral mixture analysis: A review. Remote Sens. Environ. 115, 1603–1616. https://doi.org/10.1016/j.rse.2011.03.003.
Stenberg, Pauline, 2007. Simple analytical formula for calculating average photon recollision probability in vegetation canopies. Remote Sensing of Environment 109 (2), 221–224.
Suzuki, R., Kobayashi, H., Delbart, N., Asanuma, J., Hiyama, T., 2011. NDVI responses to the forest canopy and floor from spring to summer observed by airborne spectrometer in eastern Siberia. Remote Sens. Environ. 115, 3615–3624. https://doi.org/10.1016/j.rse.2011.08.022.
Takala, T.L.H., Mõttus, M., 2016. Spatial variation of canopy PRI with shadow fraction caused by leaf-level irradiation conditions. Remote Sens. Environ. 182, 99–112. https://doi.org/10.1016/j.rse.2016.04.028.
Vanhatalo, K.M., Rautiainen, M., Stenberg, P., 2014. Monitoring the broadleaf fraction and canopy cover of boreal forests using spectral invariants. J. Quant. Spectrosc. Radiat. Transf. 133, 482–488. https://doi.org/10.1016/j.jqsrt.2013.09.011.
Zou, X., Mõttus, M., 2015. Retrieving crop leaf tilt angle from imaging spectroscopy data. Agric. For. Meteorol. 205, 73–82. https://doi.org/10.1016/j.agrformet.2015.02.016.